Bioelectrochemistry 139 (2021) 107743

Contents lists available at ScienceDirect

Bioelectrochemistry

journal homepage: www.elsevier.com/locate/bioelechem

3D "honeycomb" cell/carbon nanofiber/gelatin methacryloyl (GelMA) modified screen-printed electrode for electrochemical assessment of the combined toxicity of deoxynivalenol family mycotoxins

Kaimin Wei [a], Jiadi Sun [a,*], Qing Gao [b], Xingxing Yang [a], Yongli Ye [a], Jian Ji [a], Xiulan Sun [a,*]

[a] State Key Laboratory of Food Science and Technology, School of Food Science and Technology, National Engineering Research Center for Functional Food, Synergetic Innovation Center of Food Safety and Quality Control, Jiangnan University, Wuxi, Jiangsu 214122, People's Republic of China
[b] State Key Laboratory of Fluid Power and Mechatronic Systems, School of Mechanical Engineering, Zhejiang University, Hangzhou 310027, People's Republic of China

ARTICLE INFO

Article history:
Received 17 October 2020
Received in revised form 9 January 2021
Accepted 11 January 2021
Available online 18 January 2021

Keywords:
Deoxynivalenol
3-Acetyl-deoxynivalenol
15-Acetyl-deoxynivalenol
3D printing
Toxicity
Electrochemistry

ABSTRACT

A "honeycomb" electrochemical biosensor based on 3D printing was developed to noninvasively monitor the viability of 3D cells and evaluate the individual or combined toxicity of deoxynivalenol (DON), 3-acetyldeoxynivalenol (3-ADON), and 15-acetyldeoxynivalenol (15-ADON). Carbon nanofiber (CN)/gelatin methacryloyl (GelMA) conductive composite hydrogel with strong processability was printed on 8-channel screen-printed carbon electrodes (SPCEs) to maintain cell viability and form tight cell-to-cell contacts. A "3D honeycomb" printing infill pattern was selected in the construction of the biosensors to improve conductivity. Based on 3D printing technology, the electrochemical biosensor can prevent manual error and provide for high-throughput detection. Electrochemical impedance spectroscopy (EIS) was used to evaluate mycotoxin toxicity. The EIS response decreased with the concentration of DON, 3-ADON and 15-ADON in the range of 0.1–10, 0.05–100, and 0.1–10 μg/mL, respectively, with a limit of detection of 0.07, 0.10 and 0.06 μg/mL, respectively. Mycotoxin interactions were analyzed using the isobologram–combination index (CI) method. The electrochemical cytotoxicity evaluation result was confirmed by biological assays. Therefore, a novel method for evaluating the combined toxicity of mycotoxins is proposed, which exhibits potential for application to food safety and evaluation.

1. Introduction

Deoxynivalenol (DON) is a secondary metabolite mainly produced by *Fusarium* fungi, which typically invades all kinds of crops, including cereal crops, creates high levels of pollution and is detected with high frequency worldwide [1]. It cannot be eliminated during food processing. DON mainly affects the immune system and gastrointestinal tract, causing vomiting, gastroenteritis, and immune dysfunction. Research into the relationships between airborne transmission, degree of mold exposure and inflammatory airway disease has also attracted wide attention. According to reports, farm workers are at risk of exposure to DON when handling grain or silage[2–4]. Studies on the induction of MAPK-dependent transcription factors by DON in human cell lines indicate that the expression of ATF3 mRNA was the highest in A549 cells after DON exposure[5]. Therefore, the A549 cell line is of great significance for exploring the toxicity mechanism of DON.

Similar to DON, 3-ADON and 15-ADON are also detected with high frequency in cereals (87% and 73% 3-ADON and 15-ADON positive samples, respectively) [6]. DON may be produced with its two acetylated derivatives, and their presence can be seen in up to 10–20% of DON containing samples (EFSA, 2011). In *vivo* experiments have shown that 3-ADON is rapidly converted into DON in blood [7]. Data indicate that acetylated DON is more quickly absorbed in the intestine and thus has been considered more toxic [8]. Studies on mycotoxin toxicity often focus on the effects of individual toxins, but few studies comprehensively discuss the mechanism of action underlying toxic effects due to combined mycotoxins. With the known co-existence of multiple toxins, a method for evaluating combined toxicity with multiple toxins needs to be established.

Toxicity evaluation methods mostly rely on cell experiments in two-dimensional culture and animal experiments. Two-dimensional cell experiments present advantages such as low cost and a short evaluation cycle. The cells also exhibit a certain degree of homology with the body, but the two-dimensional cell culture environment differs from the human *in vivo* environment [9]. Toxicology experiments using animals yield results that can truly and

* Corresponding authors.
E-mail addresses: sunjiadi@jiangnan.edu.cn (J. Sun), sxlzyz@jiangnan.edu.cn (X. Sun).

https://doi.org/10.1016/j.bioelechem.2021.107743
1567-5394/

comprehensively reflect the effect of drugs on the body, these experiments entail high cost and require long experimental periods among other disadvantages. Owing to high sensitivity and portability, cell-based biosensors have recently become attractive substitutes for traditional methods. In the construction of cell sensors, cells as receptors are fixed to the interface. The magnitude of a change in signal can be used for the qualitative and quantitative analysis of drug stimulation on cells [10–12]. Compared with traditional techniques, a three-dimensional (3D) cell culture platform can simulate the microenvironment of cells *in vivo* more efficiently, and monitor the response of cells to exogenous hazards more accurately [13–16]. As a simple and miniaturized detection method, the 3D cell-based biosensor has attracted considerable attention in the toxicity evaluation of drugs and pollutants.

As a type of computer-aided technology, 3D bioprinting can produce engineered tissue in a mechanized, organized, and optimized manner. It can assemble tissue by accurately locating biomaterials and living cells layer by layer and has a high spatial control capability. 3D printing technology can be applied not only to the creation of basic arrays but in the development of complex constructs by setting different sample retention times or repeating specific printer G code commands, also without the need to produce special molds or masks for patterning. Moreover, 3D printing has led to the availability of 3D tumor array chips, which are now required for specific, on demand, drug screening for rapid throughput [17,18]. This technology is used on the development and preparation of biosensors, with the advantage of mass production, reduction of artificial error and convenient operation. Gelatin methacrylate (GelMA) hydrogel is widely used in 3D printing as a kind of bioink. It comprises natural gelatin functionalized using methacrylic anhydride, which shows good processability and biocompatibility [16,19,20]. The hydrogel can be used as an auxiliary bonding material to form a stereoscopic structure for the construction of a 3D cell environment. When prepared with culture medium, the hydrogel can provide a cell growth environment that allows cells to link with one another [21,22].

With the advantages of high sensitivity, fast response, ease of operation, and simplicity of analysis, EIS can be used to evaluate the electrochemical behavior of cytotoxicity and has been recognized as one of the most attractive label-free technologies. EIS has also been successfully used to monitor morphological changes during cell adhesion and apoptosis, as well as to determine drug cytotoxicity [23–25]. Traditional electrodes, such as gold electrodes and glassy carbon electrodes, easily become polluted and require polishing and regeneration. They are complex and time-consuming, limiting their application. Screen-printed carbon electrodes (SPCEs) are low-cost, have a wide potential range, and exhibit good chemistry [26]. However, printing carbon electrodes on paper also involve challenges, such as limited sensitivity and high electrochemical resistance. These problems are addressed using carbon-conductive nanomaterials, which are widely used in electronic devices. These nanomaterials possess distinct properties, such as rapid electron transfer, high thermal conductivity, high mechanical flexibility, and good biocompatibility [27,28]. With distinct mechanical properties and superior electrical properties, carbon nanofiber (CN) is a modified material widely used in electrochemistry [29].

In the present study, a cell electrochemical sensor based on 3D bioprinting was proposed to evaluate the individual and combined toxicity of DON, 3-ADON, and 15-ADON. GelMA provides a 3D growth environment for cells, which can better simulate *in vivo* environment and assess toxicity more accurately. Variations in electrochemical reactions caused by mycotoxins stimulating A549 cells are presented. Cell viability, reactive oxygen species (ROS) and $[Ca^{2+}]_i$ concentration were also measured; the EIS signal was found to correspond to the changes in ROS, $[Ca^{2+}]_i$ concentration, and apoptotic and necrotic cell ratios. The results indicate that the method is simple, convenient, and shows potential for high-throughput online detection analysis. The proposed method provides a promising alternative for the cytotoxic evaluation of mycotoxins.

2. Experimental procedures

2.1. Materials and apparatus

Chloroauric acid ($HAuCl_4{\cdot}4H_2O$) and toxin standards (DON, 3-ADON and 15-ADON) were purchased from Sigma-Aldrich Inc (St. Louis, MO, USA). The toxin standards were dissolved in dimethyl sulfoxide (DMSO) to make a 25 mg/mL stock solution and stored at 4 °C for further use. Carbon nanofibers (XFM60) measured 200–600 nm in diameter and 5–50 μm in length were supplied by Xian Feng Nanomaterials Technology Co., Ltd (Nanjing, China). Human lung adenocarcinoma epithelial cells (A549) were purchased from Tongpai Biological Technology Co., Ltd (Shanghai, China). Dulbecco's minimal essential medium (DMEM), fetal bovine serum (FBS), phosphate buffered saline (PBS), Dichlorodihydro-fluorescein diacetate (DCFH-DA), Calcium ion Fluorescence Probe (Fluo-3 AM), and Cell Counting Kit-8 (CCK8) were purchased from the Beyotime Biotechnology Co., Ltd (Nantong, China). All solutions were prepared with ultrapure water and all reagents were of analytical grade.

3D bioprinter (EFL-BP6601), GelMA hydrogel (EFL-GM-60) and blue light source (405 nm, 3 W) were provided by Intelligent Manufacturing Research Institute (Jiangsu, China). SPCEs were obtained from Shanghai Molybdenum Electronic Technology Co., Ltd (Shanghai, China). A CO_2 incubator (Thermo Scientific Forma Series Ⅱ Water Jacket) for cell culture was purchased from Thermo Fisher Scientific Inc (Rockford, IL, USA). Electrochemical experiments were conducted using the multichannel electrochemical workstation (Chenhua, Shanghai, China). CCK-8 and fluorescence intensity assays were performed with a microplate reader (Spectra MAX 340, Molecular Devices Co., Sunny vale, CA, USA) and FACS (Becton-Dickson, San Jose, CA, USA).

2.2. Cell culture

A549 cell culture medium was composed of high glucose DMEM and 10% FBS. The medium was changed every other day as needed to keep fresh. When the cells density reaches 10^6 cells/mL, they were used for experiments.

2.3. Preparation of GelMA bioink and 3D printed cell-based sensor

The 3D printed cell-based electrochemical sensor stepwise preparation is presented in Scheme 1. To prepare the photosensitive solution, a photo-initiator, lithium phenyl(2,4,6-trimethyl benzoyl)phosphinate (LAP) was added into the DMEM cell culture solution to a final concentration of 0.5%. The LAP solution was then dissolved in a water bath at 60 °C for 30 min in the dark. The GelMA material was added into the LAP initiator solution and then dissolved in a water bath at 60 °C for 30 min in the dark. Carbon nanofibers were added to PBS to the final concentration of 2 mg/mL. Ultrasonic treatment was then conducted for 2 h. The carbon nanofiber solution was added into the GelMA solution, and the final concentration of GelMA was 5%. Human lung cancer cells A549 were mixed with the CN/GelMA composite hydrogel, and the cell concentration was adjusted to 1×10^6 cells/mL. Biological printing ink was thus prepared.

The electrode used in this study was the screen-printed carbon electrode (a 3 mm diameter carbon working electrode, a carbon

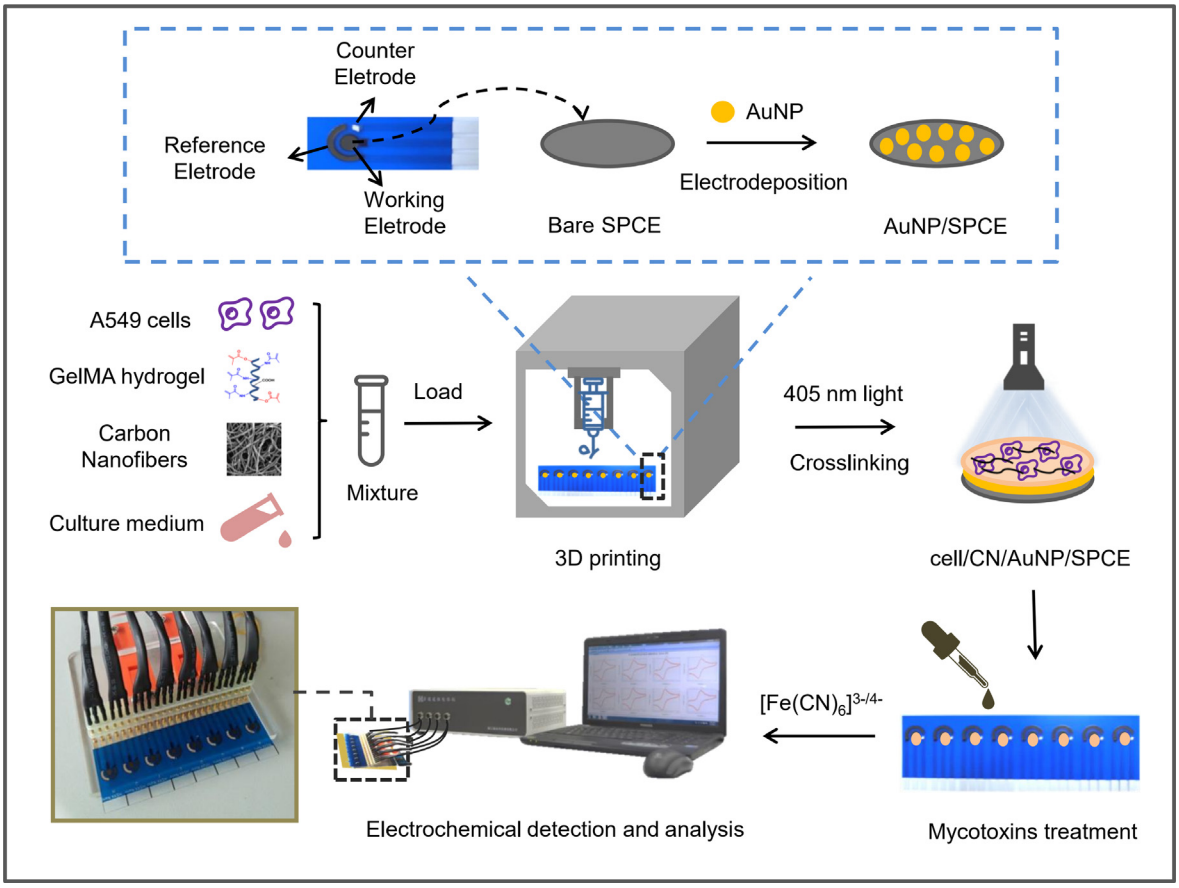

Scheme 1. Schematic representation of the route for the preparation of the 3D printed electrochemical cell-based biosensor. The dotted frame insert is the representation of the electrode modified with gold nanoparticles before 3D printing.

counter electrode, and an Ag/AgCl reference electrode). The polyethylene terephthalate substrate was printed with conductive silver ink as the first layer and conductive carbon paste as the second layer. The exposed working electrode area was then covered with an insulation layer. Bare SPCEs were activated in a 0.5 mmol/L sulfuric acid solution and scanned by cyclic voltammetry (CV) under the following conditions: voltage, −0.2 V to 0.6 V; scanning rate, 100 mV/s; and the number of scanning cycles, 8. To improve the electron transfer efficiency, the activated SPCEs were immersed in a 10 mL gold plating solution containing 1% chloroauric acid and 1 mmol/L sulfuric acid solution for gold plating. The electroplating was conducted under a voltage of −0.3 V for 160 s. The electrodes were then washed with ultrapure water and dried with nitrogen. The prepared cell/CN/GelMA composite hydrogel material was poured into the printing syringe. The printing conditions were as follows: needle barrel temperature, 23–28 °C; working platform temperature, 3 °C; extrusion pressure, 0.1 MPa; graphic diameter, 3 mm; graphic height, 0.6 mm; and spray head walking speed, 300 mm/min. The modified SPCEs were then placed in a fixed position on the working platform, and the composite hydrogel was precisely deposited on the working electrode of the screen-printed electrode by 3D printing with a "3D honeycomb" infill pattern. Immediately after 3D printing, the composite hydrogel was solidified using a 405 nm wavelength light for 10–20 s. The constructed cell sensor was incubated at 37 °C for 12 h to restore normal growth before toxicity stimulation.

2.4. Electrochemical measurements

Electrochemical experiments were conducted on the multichannel electrochemical workstation. The electrochemical behaviors of the A549 cells were studied by EIS with 2.5 mM $[Fe(CN)_6]^{3-/4-}$ and 1 M KCl as electrolytes. All electrochemical experiments were performed at room temperature. The data obtained by EIS were fitted and calculated using the software ZView. The electrochemical experiment was conducted under the following conditions: scanning range of differential pulse voltammetry (DPV), −0.2–0.6 V; scanning rate, 100 mV/s; and pulse amplitude of 0.1 V. Scanning range of cyclic voltammetry, −0.2–0.6 V; and scan rate; 0.1 V/s. The impedance spectra were recorded within a frequency range of 1–10^5 Hz. The inhibition rate of the toxin on the lung cancer cell line A549 was calculated as follows:

$$\text{Inhibition rate } (\%) = 100\left[1 - \left(R_{\text{mycotoxin}} - R_{\text{CN/GelMA}}\right)/\left(R_{\text{control}} - R_{\text{CN/GelMA}}\right)\right] \quad (1)$$

where $R_{\text{mycotoxin}}$ is the impedance of the SPCE modified using the cell/CN/GelMA composite hydrogel and stimulated using certain mycotoxin concentrations. R_{control} is the impedance of the SPCE modified using the cell/CN/GelMA composite hydrogel without toxin stimulation. $R_{\text{CN/GelMA}}$ is the impedance of the SPCE modified using the CN/GelMA composite hydrogel.

2.5. Conventional assay verification for electrochemical detection

The ROS level, intracellular Ca^{2+} concentration, apoptotic and necrotic rates were also measured to further evaluate the effects of DON, 3-ADON, and 15-ADON on A549 cells. The production of early ROS in A549 cells was monitored using a DCFH-DA probe. The intracellular Ca^{2+} levels were measured with a Fluo-3/AM, a visible wavelength calcium probe. Annexin V-FITC/PI staining combined with flow cytometry was used to identify early apoptotic

cells, late apoptotic cells, and necrotic cells. A detailed description of each experiment is provided in the Supplementary Material.

2.6. Statistical analysis

All statistical data were expressed as means ± S.D from at least triplicates and analyzed using both SPSS 16.0 and OriginPro 9. Significant differences were analyzed by one-way ANOVA and T-test procedures; if $P < 0.05$, the difference was considered statistically significant. The median-effect equation was used to model individual mycotoxin dose–response relationships [30]:

$$f_a/f_u = (D/D_m)^m \quad (2)$$

where f_a is the fraction affected by the concentration D; f_u is the unaffected fraction ($f_a = 1 - f_u$); D is the concentration; D_m is the concentration for the 50% effect; and m is the sigmoid coefficient of the dose–response curve, where $m > 1$, $m = 1$, and $m < 1$ indicate sigmoidal, hyperbolic, and negative sigmoidal dose-response curves, respectively.

Mycotoxin interactions were analyzed using the isobologram-combination index (CI) methods derived from the Chou median-effect principle [30]. This index is calculated as follows [31]:

$$^{n}(\mathrm{CI}_x)_j = \sum_{j=1}^{n} \frac{(\mathrm{D})_j}{(\mathrm{D}_x)_j} \quad (3)$$

where $(D)_j$ is the concentration required for each toxin combination to exert X% inhibition, and $(D_x)_j$ is the concentration of the toxin alone to exert X% inhibition. CI > 1.1, CI = 0.9–1.1, and CI < 0.9 indicate the type of toxin combination considered to exert an antagonistic effect, an additive effect, and a synergistic effect, respectively. The parameters for determining the inhibitory effects of individual and combined toxins on A549 cells for 48 h were calculated using the software CompuSyn.

3. Results and discussion

3.1. Characterization of screen-printed electrode constructed by 3D printing

An 8-channel "honeycomb" electrochemical biosensor was developed to evaluate the activities of 3D culture cells. Scheme 1 describes the preparation of the electrochemical sensor based on bioprinting. To improve the electrochemical sensitivity of SPCEs, gold nanoparticles (AuNPs) were electroplated on the working electrode of the SPCEs. The scanning electron microscopy (SEM) images in Fig. 1D (b) show that, the AuNPs were uniformly distributed on the electrode surface. Carbon nanofibers were incorporated to confer conductivity on the GelMA hydrogels. Fig. 1D (c) shows the uniform fixation of carbon nanofibers in the GelMA

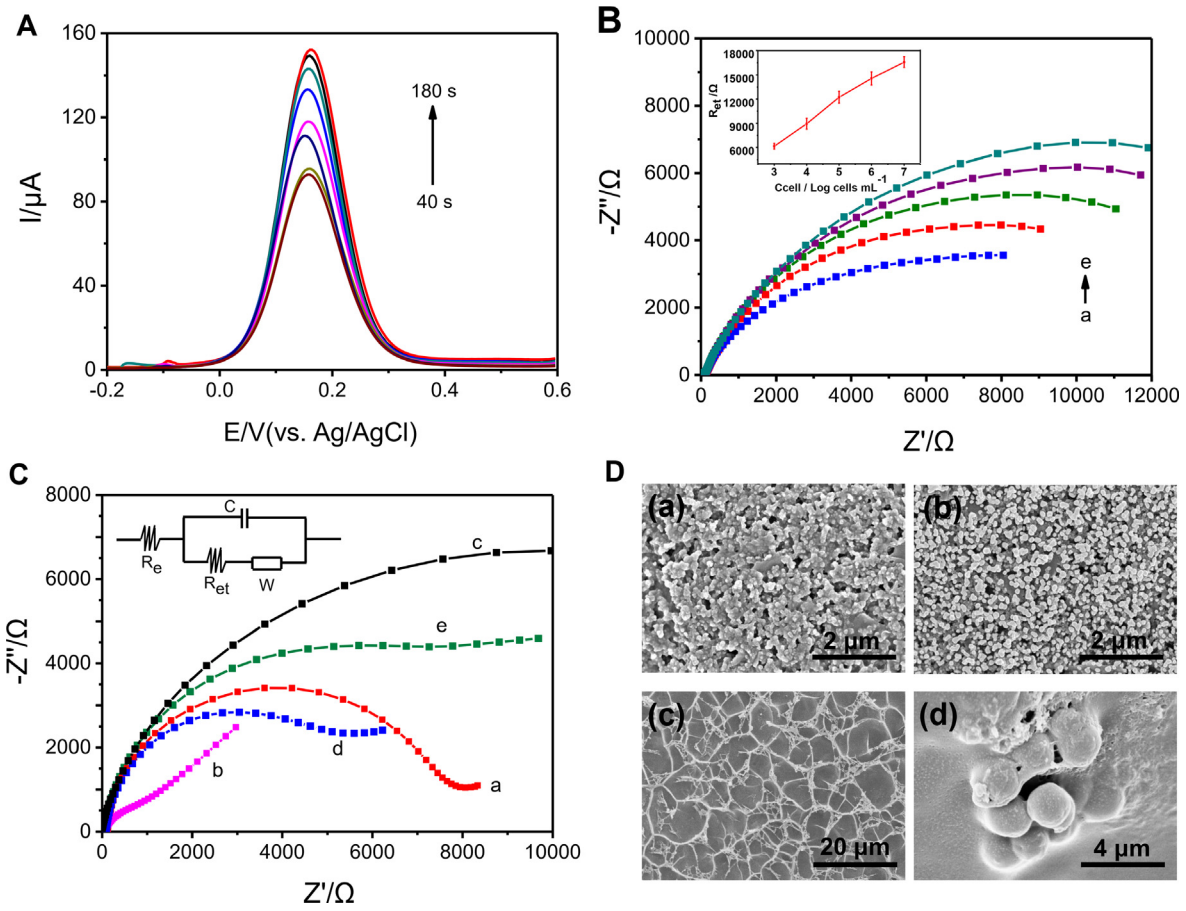

Fig. 1. Electrochemical and SEM characterization diagrams of the modified 3D cell-based biosensor. (A) Differential pulse voltammetry of AuNPs modified bare SPCE with different deposition times (time from 40 to 180 s). (B) Nyquist diagrams of 1×10^3 to 1×10^7 cells/mL (a-e) A549 cells immobilized on modified electrode. The inset shows the relationship between cell concentration and impedance. The linear regression equation was y = 2649.6 x + 3741.9 (x was the log transformed of the number of A549 cells, $R^2 = 0.9919$). (C) Nyquist diagrams of electrochemical impedance spectra of (a) bare SPCE, (b) AuNP/SPCE, (c) GelMA/AuNP/SPCE, (d) CN/GelMA/AuNP/SPCE, (e) cell/CN/GelMA/AuNP/SPCE. The insert is the equivalent circuit model, to which all of the experimental impedance curves were fitted. (D) The SEM images of the main steps in electrode fabrication. (a) bare SPCE electrode, (b) AuNP/SPCE-modified electrode, (c) CN/GelMA/AuNP/SPCE-modified electrode, (d) Cluster cells grown in CN/GelMA composite hydrogels.

hydrogel, increasing the number of catalytic active sites to improve electrochemical performance. Impedance characterization was conducted to optimize the incorporation of carbon nanofibers in the hydrogel (Fig. S1). When the A549 cells were introduced into the screen-printed carbon electrode, they were firmly fixed and evenly distributed in the CN/GelMA composite hydrogels. They were also clustered in the composite hydrogels and showed filamentous prosthesis (Fig. 1D (d)). This arrangement, confirmed the good physical condition of the cells in the hydrogel and prevented the redox probe from entering the electrode surface, thereby increasing the electron transfer resistance. When mycotoxins stimulate cells, apoptosis and cell death occur. Therefore, electron transfer accelerates the conductivity rate of the working electrode, improving the current signal.

Compared with conventional manual seeding, bioprinting can provide multiple thin cell layers, thereby inducing optimal cell growth, as they interact very closely in structure and exhibit physiological conditions similar to those that promote cell function[32]. When the printing approach was changed to manually seeded, that is, 10 μL cell/carbon nanofiber/GelMA hydrogel was dripped onto screen printing working electrode through the pipette, while other parameters remained unchanged, and the manually prepared electrochemical sensor was obtained. DPV method was used to detect the current intensity of the manually prepared and printed prepared electrochemical cell sensor, and each experimental group set up eight parallel samples. The results indicate that the current intensity of the manually prepared sensor has a large error between individuals (Fig. S3A), while the current intensity of the printed sensor is stable. Deposition of cells, carbon nanomaterials and hydrogels on screen printed electrodes by using the artificial drip method may cause the uneven distribution of cells and materials, rendering the detection inaccurate. Therefore, 3D printing can locate biomaterials and living cells more accurately, reduce human error to a certain extent, and allow mass production, with the advantages of ensuring accuracy and convenience.

3.2. Electrochemical characteristics of the 3D printed cell-based sensor

The plating time was optimized to determine the optimal amount of AuNPs to be deposited, and the conductivity levels of the electrodes with different amounts of AuNPs deposited were characterized by DPV (Fig. 1A). The optimization results indicated that when the deposition time exceeded 160 s, the peak current almost became steady; thus, 160 s was chosen as the deposition time. The concentration of A549 cells encapsulated in the GelMA hydrogel was optimized from 1×10^3 cells/mL to 1×10^7 cells/mL (Fig. 1B). The increasing diameter of the semicircle indicated that R_{et} increased, followed by an increase in cell concentration. The linear regression equation was y = 2649.6 x + 3741.9 (x was the log transformed of the number of A549 cells) with a good correlation coefficient (R^2) of 0.9919. This result suggests that with the increase in cell concentration, the barrier effect of the cell membrane on the current was enhanced, and the impedance of the cell electrochemical sensor was increased. When we consider the negative effect of the high cell density on the results accuracy as well as the number of cycles needed to obtain the cells, 1×10^6 cells/mL was selected as the appropriate number of cells to construct the cell sensor. EIS was used to test the biosensing process of the modified screen-printed electrode and the adsorption characteristics of A549 cells on the surface of the modified screen-printed carbon electrode. As shown in Fig. 1C, the Nyquist diagrams showed typical reversibility, and the levels of electron transfer impedance (R_{et}) varied with the different type of electrode modification. The R_{et} value of the bare SPCE was 7322 Ω, which significantly reduced to 965 Ω when modified with AuNPs. With the incorporation of carbon nanofibers, the R_{et} of the GelMA hydrogel on the electrode decreased from 20,990 Ω to 4309 Ω, then increased to 13,246 Ω when the cell/CN/GelMA composite hydrogels were deposited on the AuNP/SPCE surface. The hydrogel composites attached to the screen-printed electrodes inhibited the transfer of redox probes, which impeded electron transfer, thus increasing R_{et}. Owing to its high sensitivity and non-invasiveness, EIS was used to monitor the apoptosis of A549 cells on the electrode surface.

3.3. Effects of different GelMA concentrations on electrical conductivity and cell viability

The GelMA hydrogel was used to maintain cell adhesion and vitality, as well as provided a 3D cell growth environment, which could accurately simulate the changes in the electrochemical signals produced by cells *in vivo*. GelMA hydrogels with different concentrations exhibited different processing and biocompatibility characteristics, the electrical conductivity and cell viability of GelMA hydrogels with different concentrations were evaluated. Low concentrations GelMA showed extremely low viscosity (similar to that of water), whereas high concentrations GelMA exhibited extremely high viscosity, prompting the formation of wrinkled filaments at the nozzle outlet, thus failing to meet the requirements of extrusion-based 3D printing [19,33]. Therefore, the final concentrations of GelMA in the cell/CN/GelMA composite hydrogels were adjusted to 5%, 7.5%, 10%, 12.5%, and 15%, whereas the other parameters remained constant. The composite hydrogels were then deposited on the gold-plated screen-printed electrode by 3D printing. A calcein AM/propidium iodide (PI) double staining kit was used to detect cell viability after incubation for 48 h in GelMA hydrogel at different concentrations, and DPV was used to test the electrochemical signals. With an increase in GelMA concentration, the current of the screen-printed electrode decreased (Fig. 2A), indicating that GelMA at a high concentration is not conducive to electron transport. The correlation between the GelMA hydrogel concentration and redox diffusion coefficient is shown in Fig. S2. After live/dead staining, the living cells with yellow-green fluorescence and the dead cells with red fluorescence were observed at 490 ± 10 nm and 545 ± 10 nm excitation wavelength, respectively. The cell survival rate was also calculated using the counting function of the instrument. As shown in Fig. 2C, the cells grow well in the GelMA hydrogel with a low concentration (5–7.5%). Morphological changes during cell differentiation were observed, and the cells were aggregated into clusters (as shown in the red box). The A549 cells had a higher survival rate in the GelMA hydrogel with concentrations of 5–7.5%, that is, exceeding 93%. To ensure cell activity in the sensor and the 3D printing requirements, the GelMA concentration of 5% was used.

3.4. Effects of different printing infill patterns and the number of layers on electrical conductivity

Differences in printing infill patterns and the number of graphic printing layers can cause the composite hydrogel to form different morphological structures on the screen-printed electrodes, thereby affecting the electrochemical signal of the constructed sensor. In this study, the effects of 5 common printing infill patterns and different graphic printing layers on electrical signals were explored. Fig. 3A shows the 3D printed graphics of the 8-channel array and the slice models of different infill patterns. The cell/CN/GelMA composite hydrogel was printed on the screen-printed working electrode with different printing infill patterns. The CV method was used to characterize the conductivity of different infill patterns, as shown in Fig. 3B. The results showed that, the infill pattern of the "3D honeycomb" exhibited higher conductivity than that of any other infill patterns. This difference could be attributed

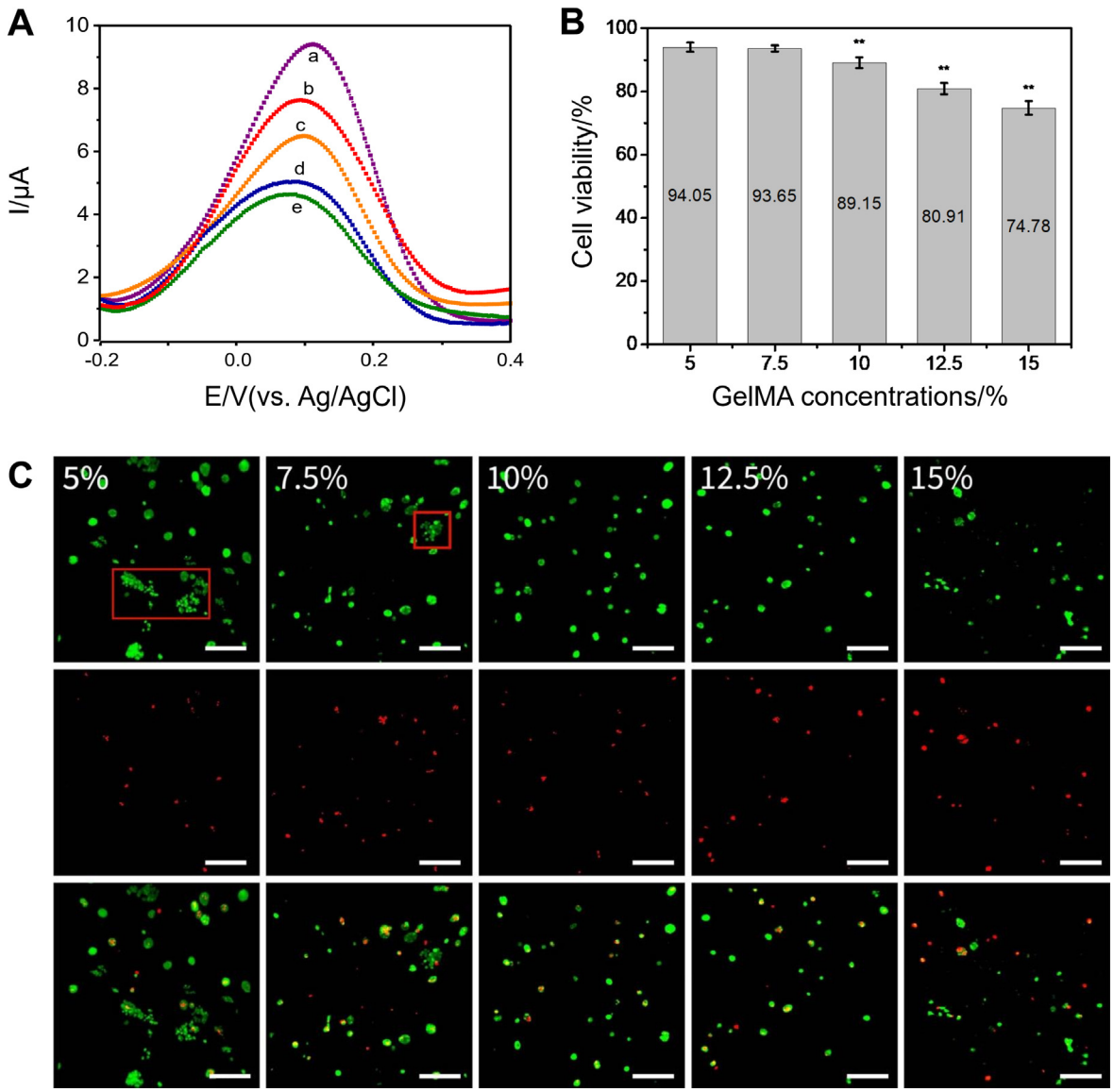

Fig. 2. Electrochemical and confocal fluorescence microscope characterization of the conductivity and biocompatibility of different GelMA concentrations. (A) Differential pulse voltammetry of GelMA hydrogels with different concentrations. (a) 5% of GelMA, (b) 7.5% of GelMA, (c) 10% of GelMA, (d) 12.5% of GelMA, (e) 15% of GelMA. (B) Survival rate of A549 cells in GelMA hydrogel with different concentrations after growth for 48 h. The asterisk indicates that the experimental group is significantly different from the lowest concentration group (** $P < 0.01$). (C) Confocal fluorogram of A549 cells in the GelMA hydrogel with different concentrations after growth for 48 h. Living cells are depicted in green, whereas dead cells are depicted in red. Scale bar = 200 μm.

to a large number of gaps in the structure that can promote electron transfer. The amounts of cells, conductive materials, nutrients, and GelMA hydrogel deposited on the screen-printed electrodes can be controlled by setting different number of graphic printing layers. The DPV method was used to characterize the effect of the number of printing layers on conductivity. As shown in Fig. 3C, the current intensity decreases with an increase in the number of printing layers. In the case of this printing graph, one layer can ensure that the composite hydrogel completely cover the surface of the working electrode. Thus, the number of printing layers selected in this study was 1.

3.5. A 3D printed cell-based sensor evaluates the toxicity of DON, 3-ADON, 15-ADON, and their combination

Electron transfer resistance is related to the number of immobilized cells on the electrode, as well as cell morphology and apoptosis [34,35]. In the present study, the modified electrode was exposed to different concentrations of DON, 3-ADON, and 15-ADON for 48 h to analyze the toxicity of each mycotoxin. Electrochemical impedance spectroscopy results are presented in Nyquist diagrams (Fig. S4). Significant changes in A549 cell impedance were observed. When the concentration of DON increased from 0.01 μg/mL to 25 μg/mL, the inhibition rate of the A549 cells increased from 4.35% to 85.96%; when the concentration of 3-ADON increased from 0.1 μg/mL to 100 μg/mL, the inhibition rate of the A549 cells increased from −1.27% to 84.58%; and when the concentration of 15-ADON increased from 0.01 μg/mL to 25 μg/mL, the inhibition rate of the A549 cells increased from 3.85% to 74.67% (Fig. 4). The LOD for DON, 3-ADON, and 15-ADON were 0.07, 0.10, and 0.06 μg/mL, calculated using the formula LOD = 3 s/m, where s represents the standard deviation of the blank sample (n = 5), and m represents the slope of the relative calibration curve for mycotoxins.

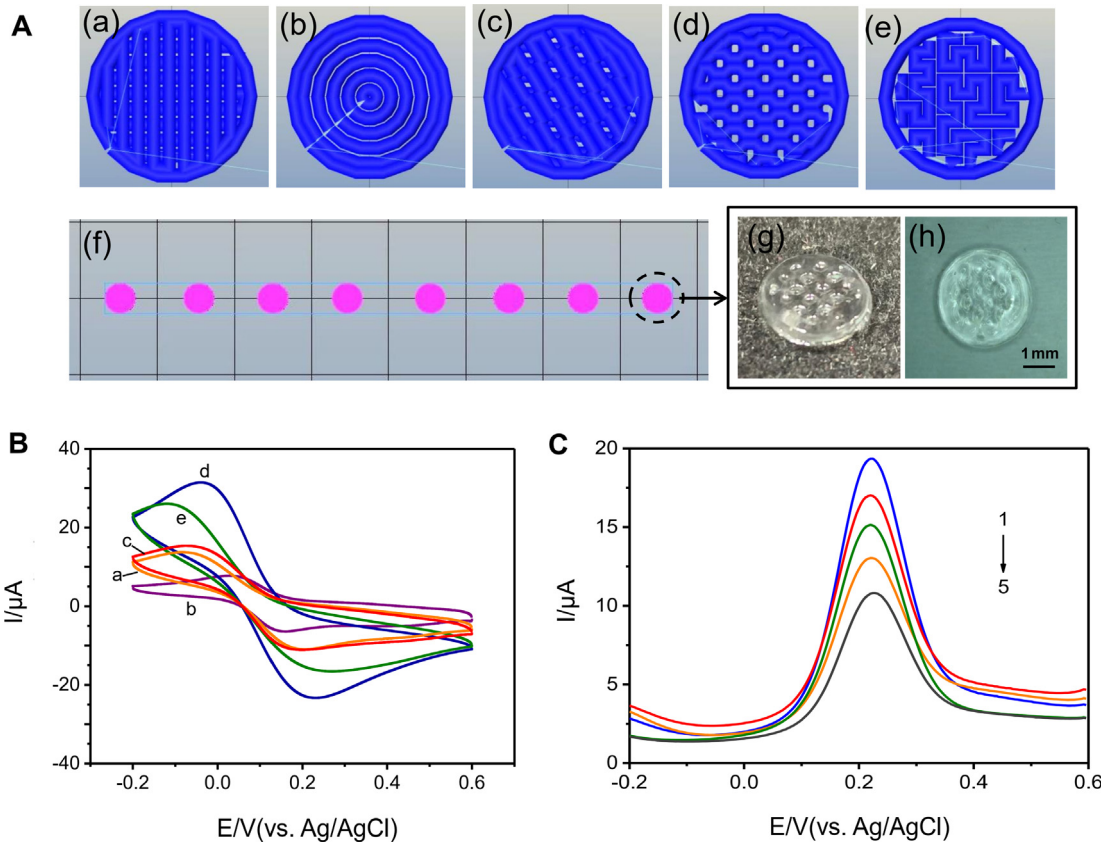

Fig. 3. Electrochemical characterization diagrams of different printing infill patterns and the number of graphic printing layers. (A) Slice models of 5 printing infill patterns and a microscope image of the 3D-printed composite GelMA hydrogel: (a) rectilinear, (b) concentric, (c) honeycomb, (d) 3D honeycomb, (e) Hilbert curve, (f) 3D-printed graph of the 8-channel array, (g) 3D-printed composite GelMA hydrogel, (h) microscope image of the 3D-printed composite GelMA hydrogel. (B) Cyclic voltammetry diagrams of the 5 printing infill patterns: (a) rectilinear, (b) concentric, (c) honeycomb, (d) 3D honeycomb, and (e) hilbert curve. (C) Differential pulse voltammetry diagrams of different numbers of printing graphic layers. The number of graphic printing layers discussed in this study was 1–5.

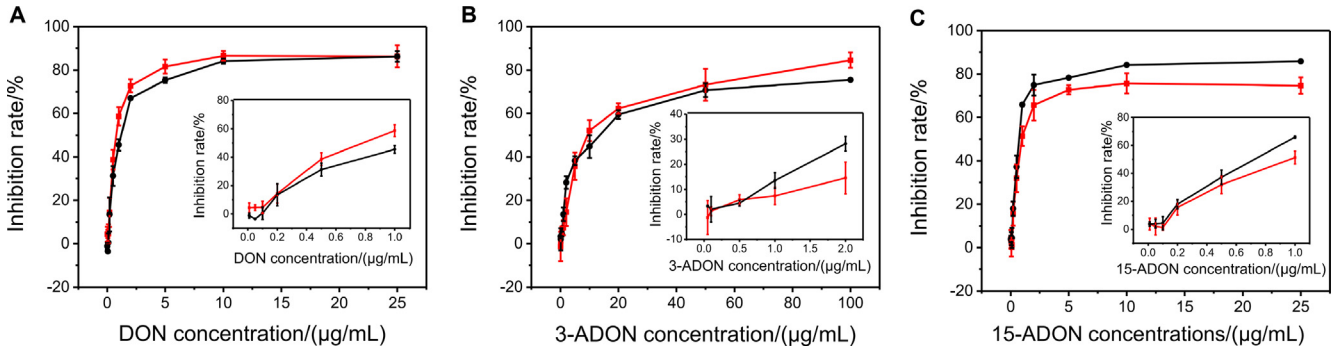

Fig. 4. Cytotoxicity curves for the A549 cells exposed to DON, 3-ADON, and 15-ADON for 48 h, as determined using the CCK-8 assay (black line) and the proposed electrochemical method (red line). (A) DON: 0.01, 0.05, 0.1, 0.2, 0.5, 1, 2, 5, 10 and 25 μg mL^{-1}. (B) 3-ADON: 0.05, 0.1, 0.5, 1, 2, 5, 10, 20, 50 and 100 μg mL^{-1}. (C) 15-ADON: 0.01, 0.05, 0.1, 0.2, 0.5, 1, 2, 5, 10 and 25 μg mL^{-1}.

The proposed electrochemical toxicity evaluation method showed that the mycotoxins decreased the activity of the A549 cells. Among the three mycotoxins DON most effectively reduced cell viability, and 3-ADON exhibited the weakest cytotoxicity. The concentrations of the mycotoxins corresponding to half-maximum cytotoxicity (IC_{50}) were as follows: DON 0.9353 μg/mL, 3-ADON 12.3194 μg/mL, and 15-ADON 1.3360 μg/mL. To evaluate the accuracy of the constructed cell electrochemical sensor, the results obtained by the proposed method were compared with those obtained using the traditional CCK-8 method, and both were found to be consistent (Fig. 4). The IC_{50} values of DON, 3-ADON, and 15-ADON obtained using the CCK-8 method were 0.9269 μg/mL, 11.9396 μg/mL, and 1.2828 μg/mL, respectively. The proposed electrochemical method is effective and can simultaneously perform multi-sample detection, whereas the traditional method is time-consuming and complex.

The combined toxicity of DON, 3-ADON and 15-ADON was evaluated. The cytotoxic effect of the combination of two or three DON family toxins at different concentration ratios, is shown in Fig. 5. CI denotes the quantitative measure of the degree of interaction of the three mycotoxins (Table 1). The results indicated that the mycotoxins sensitivity of the A549 cells is depend on the

combination of the two assays. The mixtures DON + 3-ADON, DON + 15-ADON, and DON + 3-ADON + 15-DON resulted in almost completely antagonistic cytotoxicity (IC_{10} - IC_{90}) on A549 cells. The combination of 3-ADON and 15-ADON exerted synergistic effects at low levels of cell inhibition (IC_{10}). The evaluation results of the proposed electrochemical method and CCK-8 analysis were highly similar (Table S1).

Despite the high consistency between the electrochemical cytotoxicity evaluation and the CCK-8 method, both approaches still slightly varied, which could be attributed to the differences in culture conditions and determination procedures. The toxic effect of the combined DON and 15-ADON in the current study was similar to the results obtained by Yang [36] and Juan-Garcia [37]. The differences could be related to variations in the type of cells used in these studies as well as differences in the effects exerted by mycotoxins on different organs. All results suggest that the proposed biosensor can be used as a simple and effective way to evaluate the cytotoxicity and joint toxicity of DON and its derivatives at the cellular level via EIS, compared with other methods of mycotoxin evaluation (Table S2).

Dm, m, and r represent the median-effect dose (IC_{50} value), the slope of median-effect curves and the coefficient of linear correlation derived from the experimental data according to the mass-action law. CI < 0.9, = 0.9–1.1, and >1.1 indicates synergistic, additive, and antagonistic effects, respectively.

3.6. Effects of DON, 3-ADON and 15-ADON on A549 cells

In the construction of the proposed cell-based biosensor, AuNPs and carbon nanofibers enhanced the conductivity of the hydrogel. However, the added cells weakened the electron transfer of the hydrogel, reduced the current signal, and increased the impedance. When stimulated using mycotoxins, the cells underwent apoptosis and necrosis, and the cell morphology was damaged. Therefore, the inhibitory effect of the cells on electron transfer weakened, and the impedance decreased. The SEM results indicated that when the cells were not stimulated by DON, the A549 cells retained their original shape, spread widely, whereas the A549 cells treated with mycotoxin exhibited significant morphological changes (Fig. 6E). The cell surface showed roughness and perforations, together with cytoplasmic loss. The number of cells in the sample group stimulated by toxins also decreased, and some cells became incomplete lysates. This occurrence might have caused the aforementioned decrease in impedance.

The effects of DON, 3-ADON, and 15-ADON on the production of ROS, $[Ca^{2+}]_i$ and their intrinsic cellular changes were also examined. Oxidative stress plays an important role in the toxicity of various mycotoxins, because they can cause the production of ROS in most cases. Several studies have shown that the cytotoxicity of mycotoxins is related to oxidative stress [38]. Although no previous studies have found ROS produced by DON analogs, some

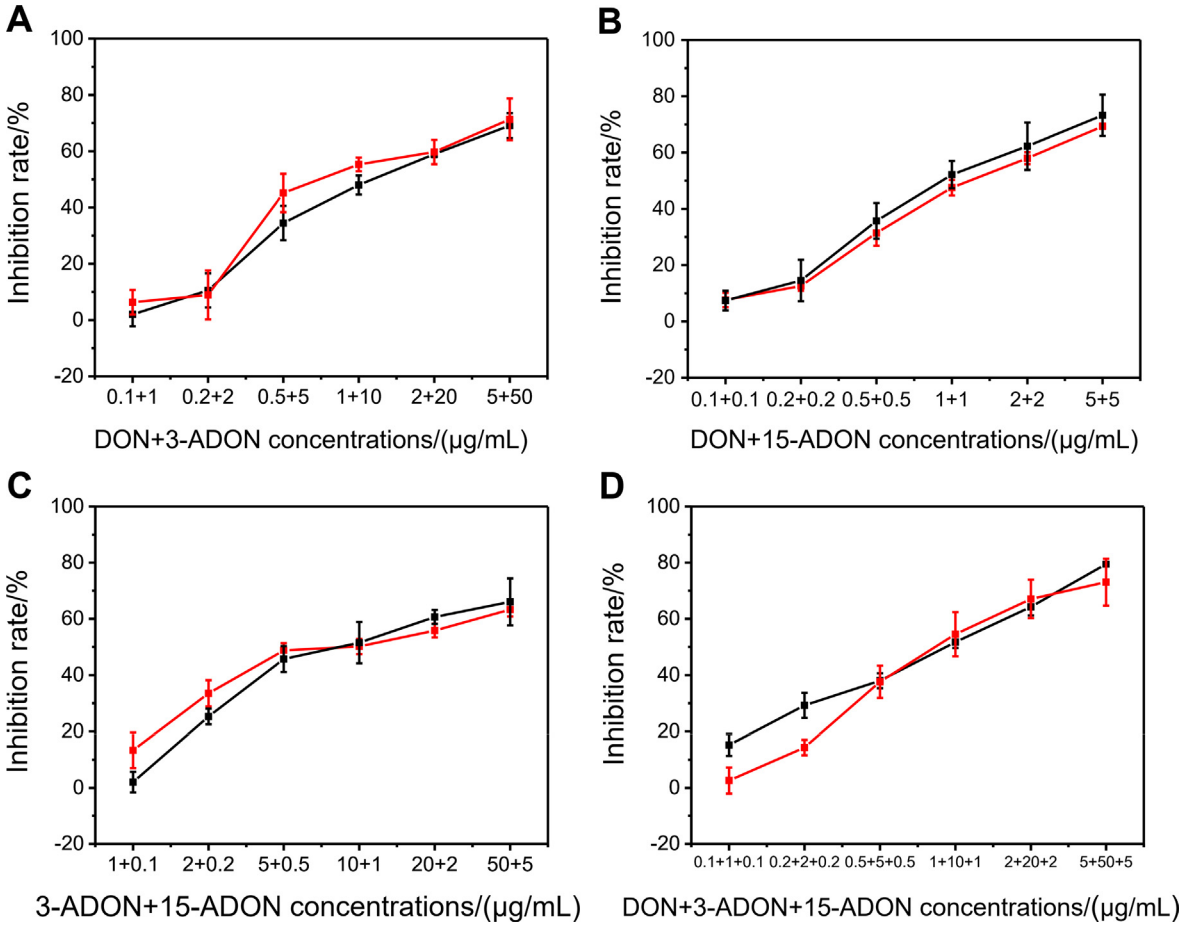

Fig. 5. Cytotoxicity curves for the A549 cells exposed to the combinations of DON, 3-ADON, and 15-ADON for 48 h, as determined using the CCK-8 assay (black line) and the proposed electrochemical method (red line). (A) DON + 3-ADON: 0.1 + 1, 0.2 + 2, 0.5 + 5, 1 + 10, 2 + 20, and 5 + 50 μg mL^{-1}. (B) DON + 15-ADON: 0.1 + 0.1, 0.2 + 0.2, 0.5 + 0.5, 1 + 1, 2 + 2, and 5 + 5 μg mL^{-1}. (C) 3-ADON + 15-ADON: 1 + 0.1, 2 + 0.2, 5 + 0.5, 10 + 1, 20 + 2, and 50 + 5 μg mL^{-1}. (D) DON + 3-ADON + 15-ADON: 0.1 + 1 + 0.1, 0.2 + 2 + 0.2, 0.5 + 5 + 0.5, 1 + 10 + 1, 2 + 20 + 2, and 5 + 50 + 5 μg mL^{-1}.

Table 1
Combination index (CI) values for different combinations of DON, 3-ADON and 15-ADON using the proposed electrochemical method.

Mycotoxin	Dose-Effect Parameters			CI Values				
	D_m (μg/mL)	m	r	10% Cytotoxicity	30% Cytotoxicity	50% Cytotoxicity	70% Cytotoxicity	90% Cytotoxicity
DON + 3-ADON	16.72	1.16	0.95	6.76	3.48	2.46	1.85	1.32
DON + 15-ADON	2.99	0.88	0.98	1.69	2.30	2.78	3.37	4.57
3-ADON + 15-ADON	13.05	0.56	0.92	0.67	1.34	2.27	4.12	11.99
DON + 3-ADON + 15-ADON	10.41	0.75	0.99	1.70	1.96	2.34	2.95	4.68

Dm, m, and r represent the median-effect dose (IC_{50} value), the slope of median-effect curves and the coefficient of linear correlation derived from the experimental data according to the mass-action law. CI < 0.9, = 0.9–1.1, and >1.1 indicates synergistic, additive, and antagonistic effects, respectively.

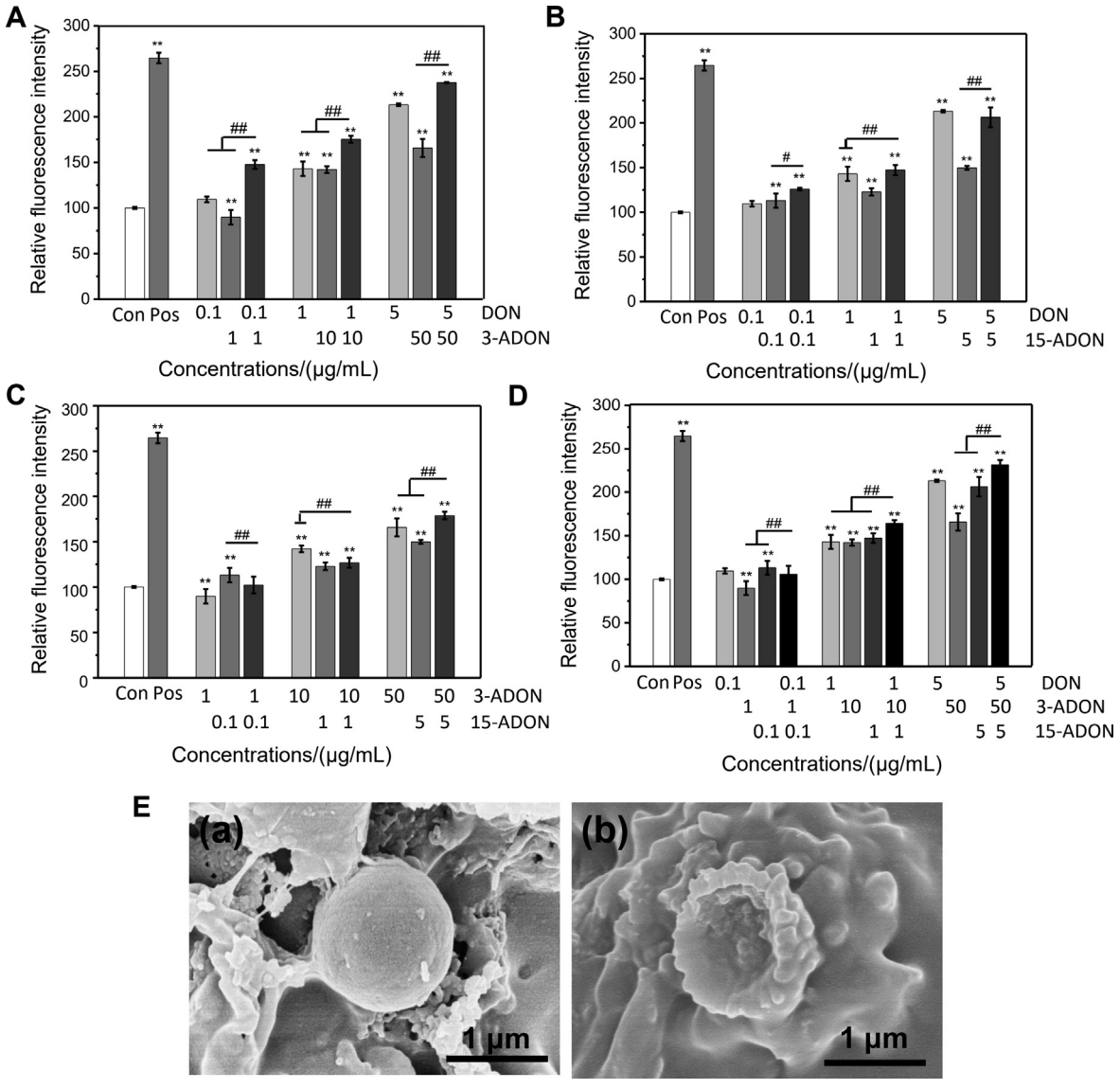

Fig. 6. (A-D) Individual and combined effects of mycotoxins on intracellular ROS production (Con, control; Pos, positive). * $P < 0.05$ and ** $P \leq 0.01$ compared with the control, and # indicates the combined toxin treatment group compared, with the single toxin treatment group, # $P < 0.05$, ## $P \leq 0.01$. The toxin dosage unit is μg mL^{-1}. (E) Morphology of the cells treated with DON for 48 h. (a) Cells without mycotoxin treatment. (b) Cells treated with 1 μg mL^{-1} DON. (In this case, the inhibition rate was approximately 50%).

studies have suggested that epoxy groups of 3-ADON and 15-ADON are mechanically bound to ribosomes, an occurrence referred to as ribotoxic stress response. This process leads to the activation of various protein kinases, regulation of gene expression, inhibition of protein synthesis, and production of cytotoxicity [39]. In addition, studies have shown that DON-induced ROS production is one of the main causes of interference with cells and genes [40]. In the current study, ROS production in A549 cells was measured when stimulated by DON, 3-ADON, and 15-ADON (Fig. 6A-6D). The DCFH-DA fluorescent probe was used to determine ROS production. Hydrogen peroxide served as a positive control. When the mycotoxins DON and 3-ADON individually stimulated the A549 cells, the average fluorescence intensity of the low-dose group did not increase significantly, whereas that of the

high-dose group increased significantly. When 15-ADON stimulated the A549 cells, the fluorescence intensity increased significantly within the selected dose range. When the mycotoxins co-stimulated the cells, the ROS level significantly increased relative to that of the control group, and the fluorescence intensity was higher than that of the individual mycotoxins, particularly in the high-dose group. This result indicates that the coexistence of mycotoxins promotes ROS production and aggravates oxidative stress in cells.

The production of $[Ca^{2+}]_i$ and the apoptosis of the A549 cells were also determined to explore the physiological changes in A549 cells after treatment with mycotoxins. Intracellular Ca^{2+} concentration is a messenger factor that regulates intracellular signaling pathways. Under normal physiologic conditions, the intracellular Ca^{2+} concentration is maintained at a considerably low level. When cells are stimulated by external chemicals, $[Ca^{2+}]_i$ homeostatic imbalance occurs, and intracellular calcium content increases. As shown in Fig. 7A, DON only slightly affects the intracellular calcium homeostasis of the A549 cells; meanwhile, the intracellular Ca^{2+} level increases after treatment with 3-ADON and 15-ADON for 48 h and increases as the toxin dose increases. The inhibition rate calculated using the EIS method showed an approximately linear relationship with the relative fluorescence intensity of calcium ions (Fig. 7B and 7C).

Phosphatidylserine is a phospholipid protein distributed on the inner side of cell membranes. When cells undergo early apoptosis, phosphatidylserine turns outward from the inside of the cell membrane. Annexin V is a phospholipid binding protein, and using FITC-labeled Annexin V as a fluorescent probe can sensitively detect early apoptotic cells. Meanwhile, the nucleic acid dye propidium iodide (PI) cannot penetrate intact cell membranes, such as those of normal and early apoptotic cells. However, PI can penetrate the cell membrane of late apoptotic cells and necrotic cells, as well as combine with the nucleus to exhibit red fluorescence. Matching Annexin V with PI can distinguish early apoptotic, late apoptotic, and necrotic cells. The effects of each of the three mycotoxins (Fig. S5) or their coexistence (Fig. S6) at selected concentrations on A549 cell apoptosis were evaluated. The percentages of the mechanically damaged cells, late apoptotic and necrotic, early apoptotic, and viable cells after stimulation by individual mycotoxins are shown in Fig. 7D-7F. Marked changes in cell profiles after mycotoxin treatment revealed a significant decrease in viable cells after treatment with DON, 3-ADON, or 15-ADON for 48 h. In addition, the rate of inhibition detected by EIS and the percentage of apoptotic and necrotic cells showed similar dose-response trends, suggesting that the migration of calcium ions and apoptotic cells affected electron transfer and enhanced the electrical signal.

4. Conclusion

Sensors for assessing cytotoxic responses are highly suitable for various sensing applications, including toxin detection and drug evaluation. Using cells as biosensors can simulate human physiological responses to a certain extent. Numerous toxicity sensors have been proposed. Most of the electrochemical cell sensors are constructed based on manual operation, which inevitably introduces human error. In this study, a simple and multi-sample electrochemical biosensor based on 3D printing was developed to evaluate the individual toxicity and combined toxicity of DON and its acetylated derivatives. A549 cells were fixed on a screen-printed carbon electrode by using a 3D printing program. The electrochemical sensitivity test provides a potential advantage over traditional analysis. The results of this study indicated that DON, 3-ADON, and 15-ADON caused significant decreases in cell viability in a dose-dependent manner. The IC_{50} values of DON, 3-ADON, and 15-ADON were 0.9352, 12.3194 and 1.3360 μg/mL, respectively. Binary mixtures of 3-ADON + 15-DON exhibited a synergistic effect at lower cytostatic rates and an antagonistic effect at higher cytostatic rates. DON + 3-ADON, DON + 15-ADON and DON + 3-ADON + 15-DON mixtures resulted in almost complete antagonistic cytotoxicity (IC_{10} - IC_{90}) on A549 cells. These results were confirmed using the CCK-8 assay. The intracellular environmental information system was related to the ROS level, intracellular Ca^{2+} concentration, as well as apoptotic and necrotic rates. After the cells were incubated with mycotoxins, apoptosis occurred, affecting the electrochemical signal. The proposed electrochemical method is simple, effective, and real-time. Moreover, it can conveniently evaluate the toxicity of mycotoxins. Further research is needed to verify long-term modified electrode storage. The proposed method is the first to present a design of an impedance sensor based on 3D bioprinting for evaluating the individual and combined toxicities of DON, 3-ADON, and 15-ADON.

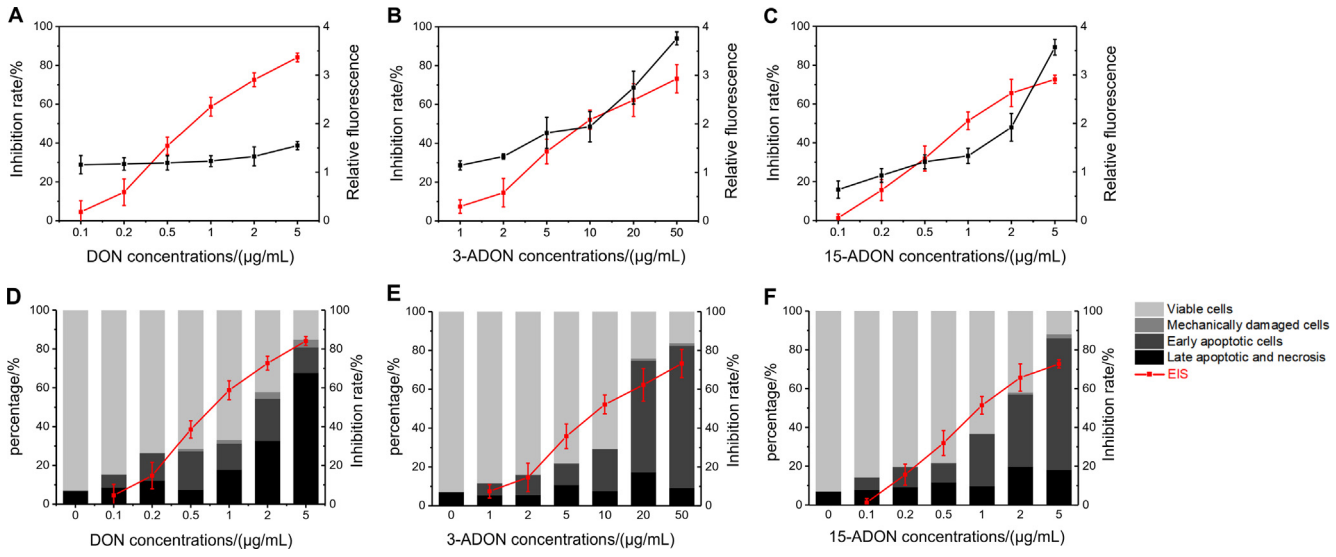

Fig. 7. Effects of DON and its acetylated derivatives on A549 cell viability, as determined using the proposed electrochemical method and biological assay. (A-C) EIS (black line) and $[Ca^{2+}]_i$ measurements (red line); (D-F) EIS and cell apoptosis.

Declaration of Competing Interest

The authors declare that they have no known competing financial interests or personal relationships that could have appeared to influence the work reported in this paper.

Acknowledgments

This work was supported by the Natural Science Foundation of China (No. 31772069, No. 31801660), the fellowship China Postdoctoral Science Foundation (2020M671343), Natural Science Foundation of Jiangsu Province (No. BK20190584), the Fundamental Research Funds for the Central Universities (10220 50205205500), National first-class discipline program of Food Science and Technology (JUFSTR20180303), Collaborative Innovation Center for Food Safety and Quality Control.

Appendix A. Supplementary material

Supplementary data to this article can be found online at https://doi.org/10.1016/j.bioelechem.2021.107743.

References

[1] F. Wu, J.D. Groopman, J.J. Pestka, Public Health Impacts of Foodborne Mycotoxins, Annu. Rev. Food Sci. T 5 (2014) 351–372.
[2] J.J. Pestka, Deoxynivalenol: mechanisms of action, human exposure, and toxicological relevance, Arch. Toxicol. 84 (2010) 663–679.
[3] S. Mayer, V. Curtui, E. Usleber, M. Gareis, Airborne mycotoxins in dust from grain elevators, Mycotoxin Res. 23 (2007) 94–100.
[4] S. Mayer, S. Engelhart, A. Kolk, H. Blome, The significance of mycotoxins in the framework of assessing workplace related risks, Mycotoxin Res. 24 (2008) 151–164.
[5] M. Casteel, C. Nielsen, A. Didier, R. Dietrich, E. Martlbauer, Induction of MAPK-dependent transcription factors by deoxynivalenol in human cell lines, Mycotoxin Res. 26 (2010) 9–14.
[6] M. De Boevre, J.D. Di Mavungu, P. Maene, K. Audenaert, D. Deforce, G. Haesaert, M. Eeckhout, A. Callebaut, F. Berthiller, C. Van Peteghem, S. De Saeger, Development and validation of an LC-MS/MS method for the simultaneous determination of deoxynivalenol, zearalenone, T-2-toxin and some masked metabolites in different cereals and cereal-derived food, Food Addit. Contam. A 29 (2012) 819–835.
[7] M. Bretz, M. Beyer, B. Cramer, H.U. Humpf, Stable isotope dilution analysis of the Fusarium mycotoxins deoxynivalenol and 3-acetyldeoxynivalenol, Mol. Nutr. Food Res. 50 (2006) 251–260.
[8] F. Berthiller, C. Dall'Asta, R. Schuhmacher, M. Lemmens, G. Adam, R. Krska, Masked mycotoxins: Determination of a deoxynivalenol glucoside in artificially and naturally contaminated wheat by liquid chromatography-tandem mass spectrometry, J. Agr. Food Chem. 53 (2005) 3421–3425.
[9] L. Ceriotti, J. Ponti, P. Colpo, E. Sabbioni, F. Rossi, Assessment of cytotoxicity by impedance spectroscopy, Biosens. Bioelectron. 22 (2007) 3057–3063.
[10] W.A. El-Said, C.H. Yea, H. Kim, B.K. Oh, J.W. Choi, Cell-based chip for the detection of anticancer effect on HeLa cells using cyclic voltammetry, Biosens. Bioelectron. 24 (2009) 1259–1265.
[11] Q. Wang, J.R. Fang, D.X. Cao, H.B. Li, K.Q. Su, N. Hu, P. Wang, An improved functional assay for rapid detection of marine toxins, saxitoxin and brevetoxin using a portable cardiomyocyte-based potential biosensor, Biosens. Bioelectron. 72 (2015) 10–17.
[12] Y. Ye, J. Ji, F. Pi, H. Yang, J. Liu, Y. Zhang, S. Xia, J. Wang, D. Xu, X. Sun, A novel electrochemical biosensor for antioxidant evaluation of phloretin based on cell-alginate/L-cysteine/gold nanoparticle-modified glassy carbon electrode, Biosens. Bioelectron. 119 (2018) 119–125.
[13] S. Xia, P. Zhu, F. Pi, Y. Zhang, Y. Li, J. Wang, X. Sun, Development of a simple and convenient cell-based electrochemical biosensor for evaluating the individual and combined toxicity of DON, ZEN, and AFB1, Biosens. Bioelectron. 97 (2017) 345–351.
[14] A.S. Barros, E.C. Costa, A.S. Nunes, D. de Melo-Diogo, I.J. Correia, Comparative study of the therapeutic effect of Doxorubicin and Resveratrol combination on 2D and 3D (spheroids) cell culture models, Int. J. Pharm. 551 (2018) 76–83.
[15] Y. Pan, N. Hu, X. Wei, L. Gong, B. Zhang, H. Wan, P. Wang, 3D cell-based biosensor for cell viability and drug assessment by 3D electric cell/matrigel-substrate impedance sensing, Biosens. Bioelectron. 130 (2019) 344–351.
[16] D. Jiang, P. Ge, L. Wang, H. Jiang, M. Yang, L. Yuan, Q. Ge, W. Fang, X. Ju, A novel electrochemical mast cell-based paper biosensor for the rapid detection of milk allergen casein, Biosens. Bioelectron. 130 (2019) 299–306.
[17] L. Cevenini, M.M. Calabretta, G. Tarantino, E. Michelini, A. Roda, Smartphone-interfaced 3D printed toxicity biosensor integrating bioluminescent "sentinel cells", Sens. Actuators, B 225 (2016) 249–257.
[18] M.A.U. Khalid, Y.S. Kim, M. Ali, B.G. Lee, Y.-J. Cho, K.H. Choi, A lung cancer-on-chip platform with integrated biosensors for physiological monitoring and toxicity assessment, Biochem. Eng. J. 155 (2020) 107469.
[19] J. Yin, M. Yan, Y. Wang, J. Fu, H. Suo, 3D Bioprinting of Low-Concentration Cell-Laden Gelatin Methacrylate (GelMA) Bioinks with a Two-Step Cross-linking Strategy, ACS Appl. Mater. Interfaces 10 (2018) 6849–6857.
[20] L. Shao, Q. Gao, C. Xie, J. Fu, M. Xiang, Y. He, Synchronous 3D Bioprinting of Large-Scale Cell-Laden Constructs with Nutrient Networks, Adv. Healthc Mater. (2019) e1901142.
[21] P. Zorlutuna, N. Annabi, G. Camci-Unal, M. Nikkhah, J.M. Cha, J.W. Nichol, A. Manbachi, H.J. Bae, S.C. Chen, A. Khademhosseini, Microfabricated Biomaterials for Engineering 3D Tissues, Adv. Mater. 24 (2012) 1782–1804.
[22] J.M. Lee, W.Y. Yeong, Design and Printing Strategies in 3D Bioprinting of Cell-Hydrogels: A Review, Adv. Healthc. Mater. 5 (2016) 2856–2865.
[23] J. Ping, Y. Wang, K. Fan, J. Wu, Y. Ying, Direct electrochemical reduction of graphene oxide on ionic liquid doped screen-printed electrode and its electrochemical biosensing application, Biosens. Bioelectron. 28 (2011) 204–209.
[24] W.S. Gu, P. Zhu, D.L. Jiang, X.X. He, Y. Li, J. Ji, L.J. Zhang, Y.G. Sun, X.L. Sun, A novel and simple cell-based electrochemical impedance biosensor for evaluating the combined toxicity of DON and ZEN, Biosens. Bioelectron. 70 (2015) 447–454.
[25] S. Hannah, E. Addington, D. Alcorn, W. Shu, P.A. Hoskisson, D.K. Corrigan, Rapid antibiotic susceptibility testing using low-cost, commercially available screen-printed electrodes, Biosens. Bioelectron. 145 (2019) 111696.
[26] P. Nicholas, R. Pittson, J.P. Hart, Development of a simple, low cost chronoamperometric assay for fructose based on a commercial graphite-nanoparticle modified screen-printed carbon electrode, Food Chem. 241 (2018) 122–126.
[27] P. Bollella, G. Fusco, C. Tortolini, G. Sanzo, G. Favero, L. Gorton, R. Antiochia, Beyond graphene: Electrochemical sensors and biosensors for biomarkers detection, Biosens. Bioelectron. 89 (2017) 152–166.
[28] P. Bollella, F. Mazzei, G. Favero, G. Fusco, R. Ludwig, L. Gorton, R. Antiochia, Improved DET communication between cellobiose dehydrogenase and a gold electrode modified with a rigid self-assembled monolayer and green metal nanoparticles: The role of an ordered nanostructuration, Biosens. Bioelectron. 88 (2017) 196–203.
[29] L. Oularbi, M. Turmine, M. El Rhazi, Electrochemical determination of traces lead ions using a new nanocomposite of polypyrrole/carbon nanofibers, J. Solid State Electr. 21 (2017) 3289–3300.
[30] T.-C. Chou, P. Talalay, Quantitative analysis of dose-effect relationships: the combined effects of multiple drugs or enzyme inhibitors, Adv. Enzyme Regul. 22 (1984) 27–55.
[31] T.C. Chou, The mass-action law based algorithms for quantitative econo-green bio-research, Integr. Biol.-Uk 3 (2011) 548–559.
[32] L. Horvath, Y. Umehara, C. Jud, F. Blank, A. Petri-Fink, B. Rothen-Rutishauser, Engineering an in vitro air-blood barrier by 3D bioprinting, Sci. Rep. 5 (2015) 7974.
[33] Q. Gao, X. Niu, L. Shao, L. Zhou, Z. Lin, A. Sun, J. Fu, Z. Chen, J. Hu, Y. Liu, Y. He, 3D printing of complex GelMA-based scaffolds with nanoclay, Biofabrication 11 (2019) 035006.
[34] N. DePaola, J.E. Phelps, L. Florez, C.R. Keese, F.L. Minnear, I. Giaever, P. Vincent, Electrical impedance of cultured endothelium under fluid flow, Ann. Biomed. Eng. 29 (2001) 648–656.
[35] X.M. Wang, P. Zhu, F.W. Pi, H. Jiang, J.D. Shao, Y.Z. Zhang, X.L. Sun, A Sensitive and simple macrophage-based electrochemical biosensor for evaluating lipopolysaccharide cytotoxicity of pathogenic bacteria, Biosens. Bioelectron. 81 (2016) 349–357.
[36] Y. Yang, S. Yu, Y. Tan, N. Liu, A. Wu, Individual and Combined Cytotoxic Effects of Co-Occurring Deoxynivalenol Family Mycotoxins on Human Gastric Epithelial Cells, Toxins (Basel) 9 (2017).
[37] A. Juan-Garcia, C. Juan, J. Tolosa, M.J. Ruiz, Effects of deoxynivalenol, 3-acetyl-deoxynivalenol and 15-acetyl-deoxynivalenol on parameters associated with oxidative stress in HepG2 cells, Mycotoxin Res. 35 (2019) 197–205.
[38] E. Ferrer, A. Juan-Garcia, G. Font, M.J. Ruiz, Reactive oxygen species induced by beauvericin, patulin and zearalenone in CHO-K1 cells, Toxicol. In Vitro 23 (2009) 1504–1509.
[39] M. Maresca, From the Gut to the Brain: Journey and Pathophysiological Effects of the Food-Associated Trichothecene Mycotoxin Deoxynivalenol, Toxins 5 (2013) 784–820.
[40] X.O. Zhang, L.P. Jiang, C.Y. Geng, J. Cao, L.F. Zhong, The role of oxidative stress in deoxynivalenol-induced DNA damage in HepG2 cells, Toxicon 54 (2009) 513–518.